Topological Properties of the Electrostatic Potential in Weak and Moderate N···H Hydrogen Bonds

Ignasi Mata,[†] Elies Molins,[†] Ibon Alkorta,[‡] and Enrique Espinosa*[,§]

Institut de Ciència de Materials de Barcelona (ICMAB−CSIC), Campus UAB, 08193 Bellaterra, Spain, Instituto de Química Médica (IQM-CSIC), Juan de la Cierva, 3, 28006 Madrid, Spain, and Laboratoire de Crystallographie et de Modélisation des Matériaux Minéraux et Biologiques, LCM[3] B, UMR CNRS 7036, Faculté des Sciences, Université Henri Poincaré - Nancy 1, BP 239, 54506 Vandoeuvre-lès-Nancy, France

Received: March 9, 2007; In Final Form: April 27, 2007

The topological analyses of the electrostatic potential $\varphi(\mathbf{r})$ and the electron density distribution $\rho(\mathbf{r})$ have been performed for a set of 20 neutral complexes with weak and moderate N···H bonds. In all cases, a zero flux surface of the electrostatic potential containing a saddle point analogous to the bond critical point of the electron density distribution is observed. These surfaces define an equivalent of the atomic basin of $\rho(\mathbf{r})$ for the electrostatic potential, which exhibits zero net charge and can be regarded as an electrostatically isolated region if its volume is finite. The $\varphi(\mathbf{r})$ and $\rho(\mathbf{r})$ zero flux surfaces divide the hydrogen-bonding region in three parts, being the central one related to the electrostatic interaction between donor and acceptor. This central region exhibits a relative size of ∼13−14% of the N···H distance d_{NH}, it belongs to the outermost shell of the nitrogen and is mainly associated with its lone pair. Topological properties of both $\rho(\mathbf{r})$ and $\varphi(\mathbf{r})$, as well as the electron kinetic (G) and potential (V) energy densities, show similar dependences with d_{NH} at both bond critical points (φ-BCP and ρ-BCP). Phenomenological proportionalities between the $\rho(\mathbf{r})$ curvatures and G and V are also found at the electrostatic potential critical point. The curvatures of the electrostatic potential, which are interpreted in terms of the electrostatic forces in the bonding region, present the same exponential dependency as the electron density distribution, to which they are related by Poisson's equation.

1. Introduction

The molecular electrostatic potential $\varphi(\mathbf{r})$[1,2] has been extensively used in the analysis of molecular reactivity due to the electrostatic character of long range interactions between molecules. In most cases, relevant features of this scalar field are found outside the molecule, its outer envelop being commonly set at 0.001 au of its electron density distribution $\rho(\mathbf{r})$. For this reason, the topological analysis of $\varphi(\mathbf{r})$ focuses in the location of critical points[3,4] and zero-flux surfaces[5] in the surroundings of the molecule, outside the bonding regions. Other molecular properties are preferred for the study of atomic binding. This is the case of $\rho(\mathbf{r})$, whose topological analysis, performed within the framework of the atoms in molecules (AIM) theory,[6] has been successfully applied to a wide range of interatomic interactions.

The topological analysis of the electrostatic potential in binding regions reveals the presence of bond critical points analogous to those of the electron density,[7] leading to a saddle point corresponding to a minimum of $\varphi(\mathbf{r})$ along the interaction bond path and a maximum in the plane perpendicular to this direction. Both the electrostatic potential at the critical point φ-BCP and the position of this point in internuclear regions appear related to properties of bonded atoms. For instance, atomic properties like atomic radius or electronegativity have been derived from the topological analysis of the electrostatic potential.[8−10] Moreover, these critical points are related to the existence of zero-flux surfaces of $\varphi(\mathbf{r})$ which define a partition of the space in basins (φ-basins) different from those obtained for the electron density (ρ-basins) as experimentally observed in crystals.[11]

In the case of hydrogen bonding interactions, the presence of $\varphi(\mathbf{r})$ bond critical points has been reported for one experimentally determined electron density distribution.[12] To our knowledge, there are no more studies on the topology of the electrostatic potential, neither experimental nor theoretical, in hydrogen bonds (HB's) that this previously referenced. This situation contrasts with the extensive number of topological analyses of the electron distribution that have been undertaken for studying this type of interaction. Thus, former experimental analyses revealed the close relationship between the $\rho(\mathbf{r})$ distribution at the HB critical point and the local electron kinetic and potential components of the energy at the same point.[13−15] Topological properties of $\rho(\mathbf{r})$ have been also appeared to be related to the interaction energy,[13,16,17] a result that has been used to retrieve an interaction potential for weak and moderate H···O hydrogen bonds.[18] Moreover, in the theoretical study of the H···F interaction, the dependence of the topological properties with the internuclear distance has been proved helpful to understand the transition from weak van der Waals interactions to strong covalent bonds.[19,20]

As the main contribution to the hydrogen bond energy is electrostatic,[21] the analysis of the electrostatic potential can be a useful complement to the rich information provided by the electron distribution. With the aim of providing insight on the electrostatic properties of the HB interactions, both $\varphi(\mathbf{r})$ and

* Corresponding author. E-mail: enrique.espinosa@lcm3b.uhp-nancy.fr
[†] Institut de Ciència de Materials de Barcelona (ICMAB−CSIC), Campus UAB.
[‡] Instituto de Química Médica (IQM-CSIC).
[§] Laboratoire de Crystallographie et de Modélisation des Matériaux Minéraux et Biologiques, LCM[3] B, UMR CNRS 7036, Faculté des Sciences, Université Henri Poincaré.

10.1021/jp071924c CCC: $37.00
Published on Web 06/21/2007

$\rho(\mathbf{r})$ have been determined by *ab initio* methods for a set of 20 X−N···H−Y complexes, and their respective topological properties have been analyzed.

This is the first study on the topology of the electrostatic potential in hydrogen-bonded complexes. In order to avoid the effect of the significant covalency that is shown up in strong hydrogen bonds, and therefore to make the interpretation easier, only weak and moderate interactions have been considered. In addition, this range of interactions is particularly of interest for a later experimental study in crystals, where weak and moderate N···H hydrogen bonds are by far much more common than the strong ones.

2. Computational Details

Calculations were performed for 20 complexes formed by one hydrogen donor (D) and one hydrogen acceptor (A) molecules linked by a N···H interaction, the hydrogen and nitrogen atoms belonging to the D and A molecules, respectively. The studied systems are the combinations of four acceptor (HCN, LiCN, N_2, and NH_3) with five donor (C_2H_2, HCl, HCN, CNH, and HF) molecules, all of them chosen in order to obtain a cylindrical symmetry in the bonding region.

The geometry of the complexes has been optimized at the MP2/6-311++G(d,p) and MP2/aug-cc-pVTZ[22] computational levels implemented in the Gaussian-03 package.[23] C_{3v} symmetry has been imposed to the complexes where NH_3 is involved, and $C_{\infty v}$ for the rest. The equilibrium geometry of the structures has been confirmed by frequency calculations. The electrostatic potential has been evaluated within the Gaussian-03 facilities at both computational levels. The electron density distribution obtained at both levels has been analyzed with the AIMPAC[24] and MORPHY98[25] programs within the AIM framework. The quality of the atomic $\rho(\mathbf{r})$ integrations has been tested by checking the value of the integrated Laplacian within the ρ-basins, which must be 0. For each monomer, the sum of atomic charges was smaller than 10^{-3} e, indicating that only small errors are present on the integrated properties.[26]

d_{NH} distances are systematically smaller for MP2/aug-cc-pVTZ than for MP2/6-311++G(d,p) (Table 1), being the largest relative difference 4.9% in the case of N_2···HCCH. The axial geometry of the studied complexes has been proved in 11 cases by microwave spectroscopy,[27−36] being the experimental d_{NH} distance closer to the values obtained with the MP2/6-311++G(d,p) calculation in ten cases. In spite the variation on the calculated distance d_{NH} from one to other computational level, the dependence of the $\rho(\mathbf{r})$ and $\varphi(\mathbf{r})$ properties on d_{NH} are similar in both computational levels. Thus, only the results from one of the basis sets (6-311++G(d,p)) will be discussed in the following section (results for aug-cc-pVTZ are given in Supporting Information). In addition, the smaller size of the 6-311++G(d,p) basis set makes it more suitable to study larger systems.

3. Results and Discussion

3.1. Zero Flux Surfaces in the Hydrogen-Bonding Region. In some aspects, the electrostatic potential $\varphi(\mathbf{r})$ and the electron density $\rho(\mathbf{r})$ topologies show equivalent features, as both scalar fields present important similarities. Indeed, both exhibit (i) local maxima at the nuclear positions[37] and (ii) (3, −1) critical points between bonded atoms,[3] indicating that topological bond critical points show up for the electrostatic potential (φ-BCP's) and for the electron density distribution (ρ-BCP). On the other hand, there are also important differences between them. Thus, while $\rho(\mathbf{r})$ can present local maxima outside the nuclear positions, this is not possible for $\varphi(\mathbf{r})$. Another important difference is that, while the electron density distribution is found positive everywhere, local accumulations of electrons (as, for example, in lone pair regions) lead to negative electrostatic potential values, appearing negative local minima of $\varphi(\mathbf{r})$ that have no counterpart in $\rho(\mathbf{r})$.

TABLE 1: N···H Distances of the Studied Complexes Observed from Both Computational Levels and from Experiments Where Values Are Sorted for the MP2/6-311++G(d,p) Calculation

	MP2/6-311++G(d,p) (Å)	MP2/aug-cc-pVTZ (Å)	experimental (Å)
H_3N···HF	1.703	1.681	1.78[a]
LiCN···HF	1.731	1.699	
LiCN···HNC	1.796	1.770	
H_3N···HNC	1.801	1.797	
H_3N···HCl	1.820	1.739	
LiCN···HCl	1.868	1.781	
HCN···HF	1.888	1.835	1.879[b]
HCN···HNC	1.982	1.932	
LiCN···HCN	2.088	2.024	
HCN···HCl	2.106	2.014	2.121[c]
H_3N···HCN	2.127	2.106	2.156[d]
N_2···HF	2.137	2.055	2.165[e]
N_2···HNC	2.235	2.171	
LiCN···HCCH	2.262	2.181	
HCN···HCN	2.265	2.188	2.224[f]
H_3N···HCCH	2.291	2.262	2.333[a]
N_2···HCl	2.360	2.297	2.417[g]
HCN···HCCH	2.417	2.321	2.406[h]
N_2···HCN	2.508	2.413	2.486[i]
N_2···HCCH	2.620	2.498	2.604[j]

[a] Reference 34. [b] Reference 27. [c] Reference 29. [d] Reference 33. [e] Reference 30. [f] Reference 28. [g] Reference 31. [h] Reference 35. [i] Reference 32. [j] Reference 36.

TABLE 2: $\varphi(\mathbf{r})$ and $\rho(\mathbf{r})$ Topological Properties of the Monomers Acting as Electron Donors

	d^a (Å)	φ^b (e Å^{-1})	q^c (e)	μ^d (e Å)
LiCN	1.315	−0.25	−1.22	1.94
NH_3	1.283	−0.21	−1.04	0.36(0.31)
HCN	1.390	−0.13	−1.02	0.62(0.62)
N_2	1.573	−0.04	0.00	0.00(0.00)

[a] Distance from the nitrogen nucleus to the minimum of electrostatic potential. [b] Value of $\varphi(\mathbf{r})$ at this point. [c] Net charge of the nitrogen. [d] Dipole moment of the monomer. Values in parenthesis correspond to experimental determinations from ref 38. The last two magnitudes have been calculated by integration of $\rho(\mathbf{r})$ within the atomic basins.

For the acceptor molecules, the presence of a lone pair suitable for the formation of a hydrogen bond is revealed by a local minimum in the electrostatic potential (Table 2). For the four studied acceptor molecules, the electrostatic potential is deeper at the minimum position as the negative charge of the nitrogen is larger. On the other side, the distance from the nitrogen nucleus and the dipole moment does not classify as these properties, as the shortest distance corresponds to NH_3 and the dipole moment of HCN is larger than that of NH_3. In spite the absence of a good correlation, both the position and the depth of the electrostatic potential well appear related to a larger electron population of the negative atom, favoring stronger N···H interactions. According to Table 1, as the minimum is closer to the nitrogen, the N···H distance tends to be shorter, a result previously observed[39] that has been used to define hydrogen bond radii.[40]

Upon formation of the complexes, the local minima of these monomers disappear, giving rise to a $\varphi(\mathbf{r})$ (3, −1) bond critical point between the nitrogen and the hydrogen atom involved in

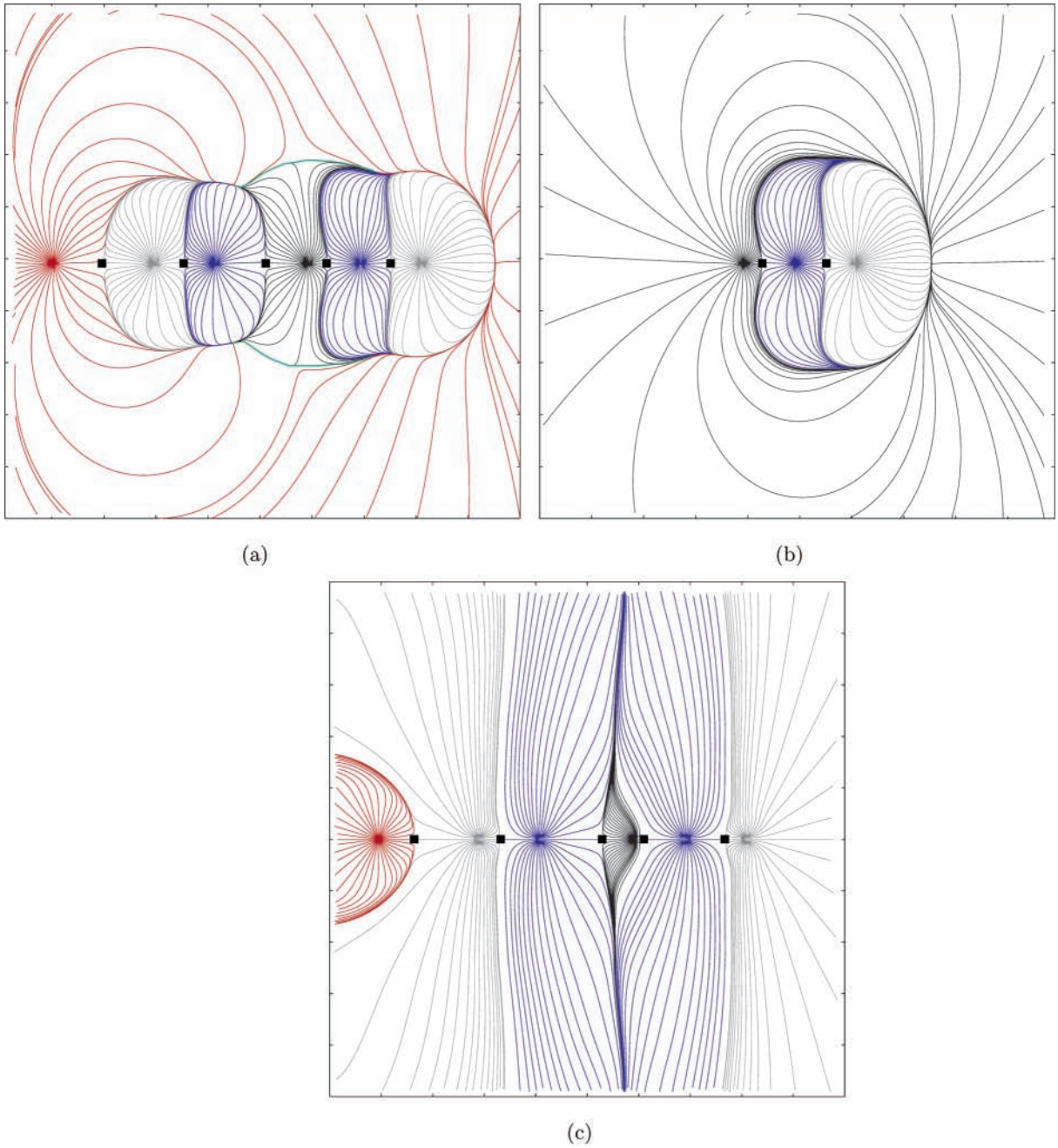

Figure 1. Electric field lines for (a) the LiCN···HNC complex and (b) the HNC monomer. (c) Gradient vector field $\nabla\rho(\mathbf{r})$ for the LiCN···HNC complex, showing the atomic basins. Ticks are in angstroms and (3, −1) critical points are denoted by black squares. Electric field lines starting at the nuclei are confined to volumes that correspond to φ-basins and are enclosed by zero-flux surfaces of $\varphi(\mathbf{r})$. φ-basins are colored according to the type of nucleus: C (grey), N (blue), H (black), and Li (red). Green lines in part a correspond to the zero-flux surface bridging both molecules. For the Li-nucleus in part a and for the H-nucleus in part b, the φ-basins extend formally up to infinity.

the hydrogen bond. In contrast to the parallel trend observed between the position of the electrostatic potential minimum in the monomers and the N···H distance in the dimers, there is no clear correspondence between the value $\varphi_{min}(\mathbf{r})$ in the monomers and that of $\varphi(\mathbf{r})$ at the φ-BCP in the dimers. φ-BCP's in hydrogen bonds were also found in a previous $\varphi(\mathbf{r})$ topological analysis derived from an experimental electron density study.[12] Like for the electron density distribution, $\varphi(\mathbf{r})$ decays from both nuclear positions along the bond direction, where the (3, −1) bond critical point is situated. As the electric field is defined as $\boldsymbol{E} = -\nabla\varphi$, two electric field lines starting at each nuclei and ending at φ-BCP define for $\varphi(\mathbf{r})$ an analogous of the $\rho(\mathbf{r})$ bond path.[11] Moreover, as $\varphi(\mathbf{r})$ at φ-BCP exhibits a local maximum in the plane perpendicular to the bond path, a set of electric field lines start at φ-BCP within this plane, defining a zero-flux surface for $\boldsymbol{E}$ between the nuclei.

These last features are shown for the LiCN···HNC complex in Figure 1. Thus, in Figure 1a, we observe the internuclear zero-flux surface in the N···H region, and the concomitant φ-BCP. Moreover, the comparison of Figure 1b and Figure 1a reveals the formation of a zero-flux surface bridging donor and acceptor molecules and surrounding the H atom. This last atom presents a finite φ-basin in the dimer, while in the monomer its φ-basin extends to infinity. A similar situation is observed in the experimental electron density of ibuprofen,[12] where the hydrogen of the carboxylate group presents an infinite φ-basin in the isolated molecule, and a finite φ-basin in the hydrogen-bonded dimer.

The Gauss theorem states that a closed surface being crossed by the same quantity of electric field lines outward than inward encloses a region with zero net charge $q = 0$. A particular case is a zero-flux surface of $\varphi(\mathbf{r})$, being impermeable to all the field lines ($\boldsymbol{E} = -\nabla\varphi$) growing inside and outside the enclosed region. This kind of surface is not therefore crossed neither outward nor inward by $\boldsymbol{E}$ lines. Closed surfaces obtained from the topological analysis of $\varphi(\mathbf{r})$ in molecular systems (hereafter φ-surfaces) are of this last type. They always enclose a unique positive punctual charge (namely, the nucleus) and each electric field line starting at its position is finishing at a critical point lying on the φ-surface, which does not belong to the formed basin (hereafter, φ-basin). Thus, the existence of a φ-surface enclosing all $\boldsymbol{E}$ lines within its associated finite φ-basin can be regarded as an electrostatic shield, avoiding the accessibility of any external charge to this region (inward) and of any internal charge to the external zone (outward). In this way, φ-basins behave as electrostatically isolated regions.

It must be noticed that, according to quantum mechanics, there is a fluctuation on the electronic population of a finite volume of the system kept fixed and two possible interpretations can be given. In the first case, it is only on a time average that finite φ-basins, considered as fixed regions, have zero net charge and are electrostatically isolated. The zero-flux surfaces and the electron populations are defined from the expectation values of the electrostatic potential and the electron density operators. Thus, any fluctuation of the electron density around its expectation value can produce a nonzero net charge on the φ-basin if the zero-flux surface is kept fixed. In the second interpretation, the fluctuation on the electron population, and therefore on the electron density distribution, leads to a concomitant fluctuation of the zero-flux surfaces limiting finite φ-basins. The volumes of the latter are thus time dependent and, at each time, they enclose a zero net charge, as stated by the Gauss theorem for this kind of systems. In this way, each observed φ-basin is the time average region over all its possible fluctuations.

The electric field lines surrounding the complex (Figure 1a) and the isolated donor monomer (Figure 1b) clearly indicate the electrostatic character of these entities. Thus, for each of them, $\boldsymbol{E}$ lines flowing from one side to the opposite one of the chemical unit typically characterize their electric dipoles, in accordance with their electrostatic description (among the complexes, LiCN···HNC exhibits the greatest dipole moment $\mu = 3.05\ e$ Å, and for HNC, $\mu = 0.69\ e$ Å).

In addition, it should be noted that the absence of monopolar moment in both cases is revealed by the flux of $\boldsymbol{E}$ lines observed outside the molecule or complex, as the total flux of any surface far enough to enclose all the electron density in the system is zero. For the φ-basins extending to infinity, we observed $\boldsymbol{E}$ lines flowing from positively charged sources to negatively charged traps.

On the other hand, due to the formation of a φ-basin with a finite volume enclosing the hydrogen nucleus in the complex, the donor molecule in LiCN···HNC is surrounded by a zero-flux surface of $\varphi(\mathbf{r})$ (Figure 1a). This appears related to the charge transfer between the interacting molecules in the complex, which charges negatively the donor and leads to the formation of a molecular φ-surface enclosing the electron distribution that completely screens the positive charge of the nuclei. As seen in the electrostatic potential of ionic crystals,[11] the φ-basins of the anions appear contracted while most of the volume of the crystal is filled by the φ-basins of the cations, as a consequence of the charge transfer between ions. The zero-flux surface enclosing the donor molecule is analogous to the zero-flux surface surrounding anions,[5] in spite the donor molecule is only partially charged. This surface has been assimilated to ionic radii,[5] but this assumption seems not to hold for ionic crystals.[11]

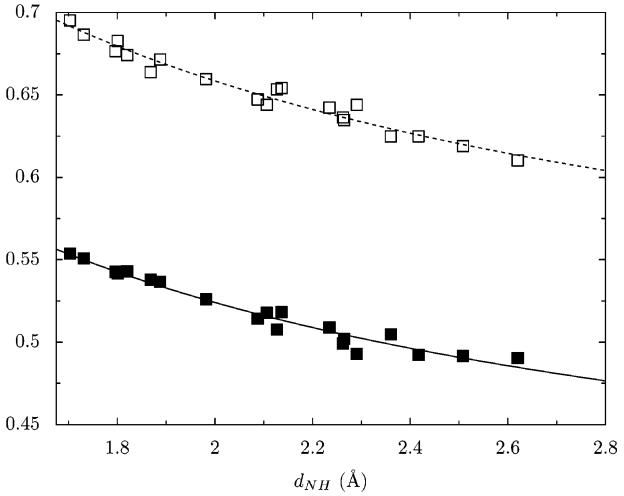

Figure 2. Relative positions of φ-BCP (black symbols and solid line) and ρ-BCP (white symbols and dashed line), respectively defined as $d_{N\varphi}/d_{NH}$ and $d_{N\rho}/d_{NH}$, *vs* the N···H distance (d_{NH}). The curves are calculated from the linear dependences of $d_{N\varphi}$ and $d_{N\rho}$ with d_{NH}.

For all complexes, the φ-surface and φ-BCP in the HB region are closer to the nitrogen nucleus than the ρ-surface and ρ-BCP due to the negative net charge of this atom. The position of both critical points, identified by the distances from the nitrogen nucleus ($d_{N\varphi}$ and $d_{N\rho}$), show a linear dependence with the bond distance (d_{NH}): $d_{N\varphi} = 0.358(8)d_{NH} + 0.33(2)$ and $d_{N\rho} = 0.468(8)d_{NH} + 0.38(2)$ (correlation factors $R^2 = 0.9907$ and 0.9942, respectively). As the interaction becomes stronger, the electronic shells of the nitrogen and hydrogen atoms are more compressed within the internuclear region. This compression pushes both the electrostatic and the atomic surfaces toward the hydrogen nucleus, as shown by the shift of the relative positions of both BCP's, given by $d_{N\varphi}/d_{NH}$ and $d_{N\rho}/d_{NH}$ in Figure 2.

As seen in this last figure, the distance between both relative positions remains approximately constant in spite of their shift toward the hydrogen nucleus when strengthening the N···H interaction. The relative size of the region comprised between both critical points ($(d_{N\rho} - d_{N\varphi})/d_{NH}$) ranges between 0.13 and 0.14 for our data set. The last result indicates that ~13−14% of the internuclear region, which belongs to the ρ-basin of the nitrogen atom and is mainly populated by its lone pair, is involved on the electrostatic interaction with the positively charged hydrogen atom (Figure 3). Thus, the attractive N···H electrostatic interaction takes place mainly inside the φ-basin enclosing the H-nucleus.

As shown in Figure 3, the $\varphi(\mathbf{r})$ zero-flux surface is closer to the N-nucleus than that of $\rho(\mathbf{r})$, and the full N···H internuclear space can be therefore divided in three regions. Region I, which is limited by the φ-surface, involves the region where $\rho(\mathbf{r})$ screens completely the N-nucleus. Regions II and III, which enclose the H-nucleus, correspond to the $\rho(\mathbf{r})$ distribution comprised between the zero-flux surfaces of $\varphi(\mathbf{r})$ and $\rho(\mathbf{r})$, being mainly associated with the nitrogen lone pair, and to the positively charged basin of the hydrogen atom. As far as the complete volume occupied by these two last regions is limited by a $\varphi(\mathbf{r})$ zero-flux surface, and region II is associated with a negative charge distribution, then $q_{II} < 0$ and this net charge must be the exact counterpart of that of region III (i.e., $q_{II} = -q_{III}$). It is pointed out that formally $q_{II} \neq q$ (N) and $q_{III} \neq q$ (H),

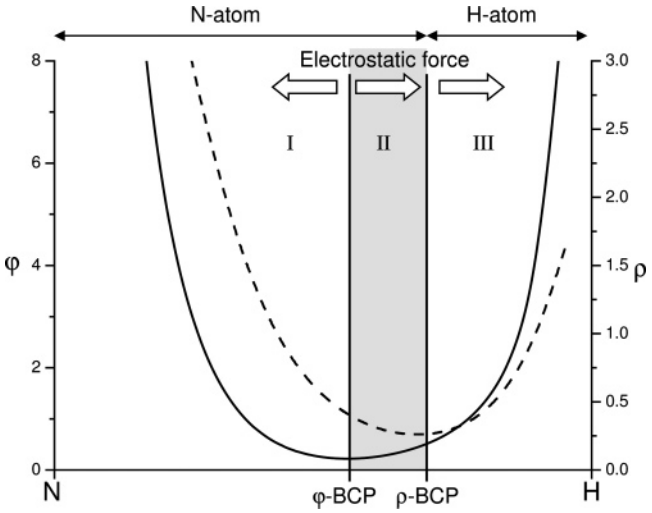

Figure 3. $\varphi(\mathbf{r})$ (solid line) and $\rho(\mathbf{r})$ (dashed line) profiles along the N···H bond axis in the LiCN···HCN complex. The complete N···H internuclear space can be divided in two electrostatic φ-basins and three regions: region I, corresponding to the first φ-basin, and regions II and III, corresponding to the second one. As far as $q = \int_\Omega \rho(\mathbf{r})\, d\Omega = 0$ for the finite φ-basins (Gauss theorem): $q_I = 0$ and $q_{II} = -q_{III}$. The intermediate region II comprised between both BCP's is in grey and represents a relative size $(d_{N\rho} - d_{N\varphi})/d_{NH}$ of $\sim 0.13 - 0.14$. The electron distribution occupying region II is responsible for the attractive electrostatic force exerted on the positively charged hydrogen basin at the ρ-surface. At φ-BCP the electrostatic force vanishes, as $\nabla\varphi = 0$. $\varphi(\mathbf{r})$ and $\rho(\mathbf{r})$ are given in e Å^{-1} and e Å^{-3}, respectively.

as the N-basin extends out the φ-basin and the latter extends out the H-basin in the complex (see Figure 1, parts a and c), even if close correspondences $q_{II} \approx q(N)$ and $q_{III} \approx q(H)$ can be established.

3.2. The Curvatures of the Electrostatic Potential. The molecular electrostatic potential is the superposition of the bare nuclear potential ($\varphi_n(\mathbf{r})$), defined as the electrostatic potential generated by the nuclei, and the contribution of the electrons. The attraction of the nuclei is the main force conditioning the electron distribution in the molecule, to the point that a close similarity exists between the topologies of $\varphi_n(\mathbf{r})$ and $\rho(\mathbf{r})$.[41] Thus, $\varphi_n(\mathbf{r})$ presents a (3, −1) critical point in all the studied complexes that is found at a distance less than 0.1 Å from ρ-BCP, the atomic basins almost matching with the electrostatic influence zones of the interacting nuclei in the hydrogen-bonding region.

The addition of the negative electronic contribution to the always positive $\varphi_n(\mathbf{r})$ distribution results in a decrease of the potential that becomes negative in the hydrogen-bonding region for three complexes (H_3N···HCCH, HCN···HCCH, and LiCN···HCCH). As observed in most cases,[7] the electronic contribution has no qualitative effect on the topology in the bonding regions, and both $\varphi_n(\mathbf{r})$ and $\varphi(\mathbf{r})$ present a (3, −1) critical point in the internuclear region. However, due to the largest screening of the N-nucleus, φ-BCP is shifted toward this atom, resulting in the separation between φ-BCP and ρ-BCP and in the formation of the intermediate region described in the previous section.

As in the case of the electron density, diagonalization of the Hessian matrix of $\varphi(\mathbf{r})$ at any point of the bond axis, and in particular at φ-BCP and at ρ-BCP, yields to one positive ($\gamma_{||}$) and to two negative eigenvalues (here both are equal to $\gamma_\perp$ due to the actual symmetry of the systems), which represent the three main curvatures of $\varphi(\mathbf{r})$ at that given point. At φ-BCP and ρ-BCP, $\gamma_{||}$ and $\gamma_\perp$ decay exponentially with d_{NH} (Figure 4),

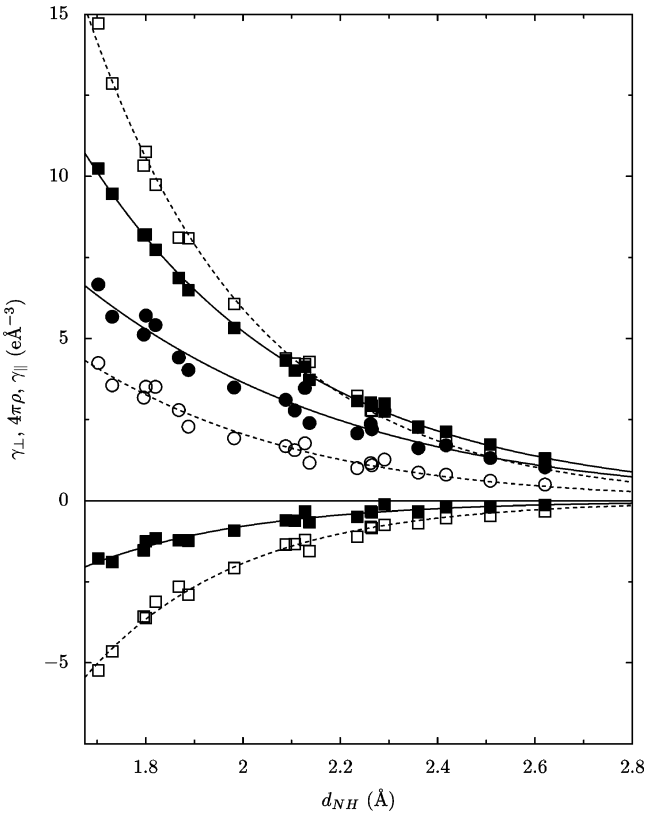

Figure 4. $\gamma_{||}$, $\gamma_\perp$ (squares), and $4\pi\rho$ (circles) *vs* d_{NH} at φ-BCP (black symbols, solid lines) and at ρ-BCP (white symbols, dashed lines). For $\gamma_{||}$ and $\gamma_\perp$, the exponential curves have been obtained from the fitting parameters given in Table 3, while for $4\pi\rho$ they have been derived from the exponential dependencies of $\gamma_{||}$ and $\gamma_\perp$ and eq 2. The curves derived for $4\pi\rho$ from the fittings indicated in Table 3 match exactly those represented here.

TABLE 3: Fittings of Topological and Energetic Properties at Both Critical Points

	φ-BCP			ρ-BCP		
y[a]	a	b (Å^{-1})	R^2	a	b (Å^{-1})	R^2
$\gamma_{||}$ (e Å^{-1})	440(20)	2.22(3)	0.998	20(2) 10^2	2.91(6)	0.996
$\gamma_\perp$ (e Å^{-1})	−190(70)	2.9(2)	0.956	−11(2) 10^2	3.2(1)	0.989
	−73(3)	[b]	0.953	−680(10)	[b]	0.986
ρ (e Å^{-3})	13(3)	1.9(1)	0.960	19(4)	2.4(1)	0.969
	23.2(6)	[b]	0.960	50(1)	[b]	0.959
$\lambda_{||}$ (e Å^{-5})	126(9)	1.59(4)	0.992	400(30)	2.40(5)	0.996
$\lambda_\perp$ (e Å^{-5})	−160(40)	2.4(2)	0.972	−5(1) 10^2	3.2(2)	0.979
G (kJ mol$^{-1}a_0^{-3}$)	20(2)10^2	1.64(5)	0.989	7570(70)	2.54(5)	0.995
V (kJ mol$^{-1}a_0^{-3}$)	−8(2)10^4	2.3(1)	0.969	−9(3) 10^4	3.8(2)	0.988

[a] Properties fitted to unweighted exponentials of the form $y = a \exp(-bd_{NH})$, where a and b are the fitted parameters. [b] b parameter fixed to the value of $\gamma_{||}$.

being the correlation factor of the fitted exponentials much better for the parallel than for the perpendicular curvature (Table 3).

The negative of $\gamma_{||}$ and of $\gamma_\perp$ are the derivatives of the electric field in the directions parallel and perpendicular to the bond. At shorter d_{NH} distances, variations of the electric field are more important because (i) the distances to the nuclei are reduced and (ii) since the electrons are confined in a smaller volume, the electron density is larger. The relationship between the electron density and the curvatures of $\varphi(\mathbf{r})$ is given by Poisson's equation (Gauss system)

$$\nabla^2\varphi(\mathbf{r}) = -4\pi \sum_\alpha Z_\alpha \delta(\mathbf{r} - \mathbf{r}_\alpha) + 4\pi\rho(\mathbf{r}) \qquad (1)$$

where Z_α and $\mathbf{r}_\alpha$ are the atomic number and the position of the

atom α and $\delta(\mathbf{r})$ is the Dirac delta. According to this relationship, at positions other than nuclear $\nabla^2\varphi(\mathbf{r})$ is always positive and hence no local concentrations of $\varphi(\mathbf{r})$ can appear. At the critical points, Poisson's equation leads, after diagonalization of the $\nabla^2\varphi$ Hessian matrix, to

$$4\pi\rho = \gamma_{||} + 2\gamma_{\perp} \tag{2}$$

where ρ is the electron density magnitude. The electron density at both φ-BCP and ρ-BCP presents an exponential dependence with the internuclear distance that appears closely related to the dependences of both $\gamma_{||}$ and $\gamma_{\perp}$ (Figure 4). Thus, the exponential increase of $\gamma_{||}$ and $\gamma_{\perp}$ as d_{NH} decreases implies a larger split of the values $\gamma_{||}$ and $2|\gamma_{\perp}|$ that results, according to eq 2, in an exponential increase of ρ at the critical points.

If ρ, $\gamma_{||}$ and $\gamma_{\perp}$ present a $y = ae^{-bd_{NH}}$ dependence, the b parameter for the three magnitudes should be the same according to eq 2. As the correlation factor is clearly better for $\gamma_{||}$ in the exponential fits of Table 3 at both critical points, a new exponential fit was performed for $\gamma_{\perp}$ and ρ with b fixed at the value for $\gamma_{||}$. As seen in Table 3 and in Figure 4, a single b parameter can be used for describing the exponential decay of the three magnitudes $\gamma_{||}$, $\gamma_{\perp}$ and ρ. Moreover, their corresponding coefficients a ($a_{||}$, $a_{\perp}$, and a_{ρ}, respectively) fulfill the condition $4\pi a_{\rho} = a_{||} + 2a_{\perp}$, according to Poisson's equation. Thus, an exponential dependence that successfully describe the evolution of ρ for the studied complexes can be derived from $\gamma_{||}$ and $\gamma_{\perp}$.

The curvatures $\gamma_{||}$ and $\gamma_{\perp}$ are related to the electrostatic force $\boldsymbol{F}_e(\mathbf{r})$, which is a component of the total force experienced by the electrons[42]

$$\mathbf{F}(\mathbf{r}) = -\rho(\mathbf{r})\sum_{\alpha} Z_{\alpha}\frac{\mathbf{r}-\mathbf{r}_{\alpha}}{|\mathbf{r}-\mathbf{r}_{\alpha}|^3} + \int \mathrm{d}^3r'\,\rho(\mathbf{r},\mathbf{r}')\frac{\mathbf{r}-\mathbf{r}'}{|\mathbf{r}-\mathbf{r}'|^3} \tag{3}$$

Here, $\rho(\mathbf{r},\mathbf{r}')$ is the electron pair density and can be decomposed as

$$\rho(\mathbf{r},\mathbf{r}') = \rho(\mathbf{r})\rho(\mathbf{r}') + \rho_{XC}(\mathbf{r},\mathbf{r}') \tag{4}$$

where exchange and correlation effects are contained in $\rho_{XC}(\mathbf{r},\mathbf{r}')$. By using this decomposition, $\boldsymbol{F}(\mathbf{r})$ can be expressed as the sum of conservative and nonconservative terms. The conservative term is the electrostatic force

$$\mathbf{F}_e(\mathbf{r}) = \rho(\mathbf{r})\left(\sum_{\alpha}\frac{Z_{\alpha}}{|\mathbf{r}-\mathrm{r}_{\alpha}|} - \int \mathrm{d}^3r'\,\frac{\rho(\mathbf{r}')}{|\mathbf{r}-\mathbf{r}'|}\right) = -\rho(\mathbf{r})\boldsymbol{E}(\mathbf{r}) \tag{5}$$

which vanishes at φ-BCP. A more correct form of $\mathbf{F}_e(\mathbf{r})$ would include a factor $(N-1)/N$ (N being the number of electrons of the system) multiplying the integral of eq 5.[43] This term takes account of the fact that an electron does not interact with itself. In the systems considered here, $(N-1)/N$ factors are within the range 0.95−0.97, and no important differences are expected between both definitions of the electrostatic force.

In the immediate surroundings of φ-BCP, the electrostatic force can be expressed as

$$\mathbf{F}_e(\mathbf{r}) = \rho(\mathbf{r})(\gamma_{||}(z-z_0)\hat{\mathbf{z}} + \gamma_{\perp} r\hat{\mathbf{r}}) \tag{6}$$

where cylindrical symmetry is supposed, z_0 is the position of φ-BCP in the bond axis, and $\hat{\mathbf{z}}$ and $\hat{\mathbf{r}}$ are unit vectors in the directions parallel and perpendicular to the bond, respectively.

As the nuclei behave as a set of positive point charges, their contribution to $\varphi(\mathbf{r})$ lead to the Laplace's equation $\nabla^2\varphi_n(\mathbf{r}) = 0$ in all the space but the nuclear positions. Therefore, the nuclear contributions to $\gamma_{||}$ and $\gamma_{\perp}$ ($\gamma_{n,||}$ and $\gamma_{n,\perp}$) must fulfill the condition

$$\gamma_{n,||} = 2|\gamma_{n,\perp}| \tag{7}$$

at φ-BCP. As a consequence, both $\gamma_{n,||}$ and $2|\gamma_{n,\perp}|$ must show the same dependency with d_{NH}. According to the sign of the curvatures and to eq 6, the electrostatic force exerted by the φ-basins points outward φ-BCP along the hydrogen bond direction and inward in the perpendicular plane to that direction, being the force constant in the parallel direction $\gamma_{n,||}$ twice than $\gamma_{n,\perp}$ in the perpendicular one.

The contribution of the electron density distribution outside the bonding region reduce the curvatures originated by the nuclei at φ-BCP, as the electrostatic force resulting from the interaction with these electrons points in opposite direction to the interaction with the nuclei. On the other side, the electrostatic force exerted by the electron distribution around φ-BCP points outward the latter in all directions, therefore increasing $\gamma_{||}$ while decreasing $\gamma_{\perp}$. Following this description, the contribution of the nuclei and the electron distribution outside the bonding region produces the increase of $\gamma_{||}$ and $\gamma_{\perp}$ as d_{NH} decreases, while the contribution of the electron distribution in the bonding region produces the splitting of $\gamma_{||}$ and $2|\gamma_{\perp}|$ required by eq 2, making the electrostatic potential (i) flatter in the perpendicular plane, and (ii) sharper along the bond direction, as shown by the small $|\gamma_{\perp}|$ and large $\gamma_{||}$ magnitudes, respectively.

According to the similarity on the exponential dependences of $\gamma_{||}$, $\gamma_{\perp}$, and ρ, proportional relationships are expected between these magnitudes, being the proportionality constants easily derived from the a coefficients in Table 3. Thus, a linear relationship is clearly observed between $\gamma_{||}$ and $\gamma_{\perp}$ at both critical points (Figure 5a), being the slope in variance with the expected value (−0.34(5) and −0.17(1) at ρ-BCP and φ-BCP respectively) and the independent term in the limit of three times its standard deviation. On the other side, the fit for the linear relationship of ρ vs $\gamma_{\perp}$ presents a slope smaller than the expected values of −0.073(2) and −0.32(2) at ρ-BCP and φ-BCP respectively, a significant independent term in both cases, and a poor R^2 factor at φ-BCP (Figure 5b).

The dependence of the topological properties with the bonding distance is given, in first approximation, by the pair of interacting atoms. The rest of the system, which in the case of the complexes corresponds to the rest of the acceptor and donor molecules, modify the properties of these atoms, tuning the form of these dependences. Thus, each of the studied complexes present a slightly different set of curves describing the variation of the topological properties with d_{NH}. For each complex, a single point corresponding to its equilibrium distance is included in the derivation of the dependences with d_{NH} for the whole set of complexes, which are therefore an average of the curves of the individual complexes.

As in the case of $\rho(\mathbf{r})$, the perpendicular curvature of $\varphi(\mathbf{r})$ presents a larger scattering around its dependence with the interatomic distance than the parallel one. Thus, the $\gamma_{||}$ and $\lambda_{||}$ curves obtained for the individual complexes are very similar, while larger differences between complexes are observed for the dependences of $\gamma_{\perp}$ and $\lambda_{\perp}$. Accordingly, it is interpreted that, while the parallel curvatures of both $\rho(\mathbf{r})$ and $\varphi(\mathbf{r})$ depend mainly on the two interacting atoms, the perpendicular ones are more affected by the environment, respresented by the rest of the atoms in the complex.

As for $\gamma_{\perp}$, the electron density at both critical points presents an important scattering around the exponential dependence with

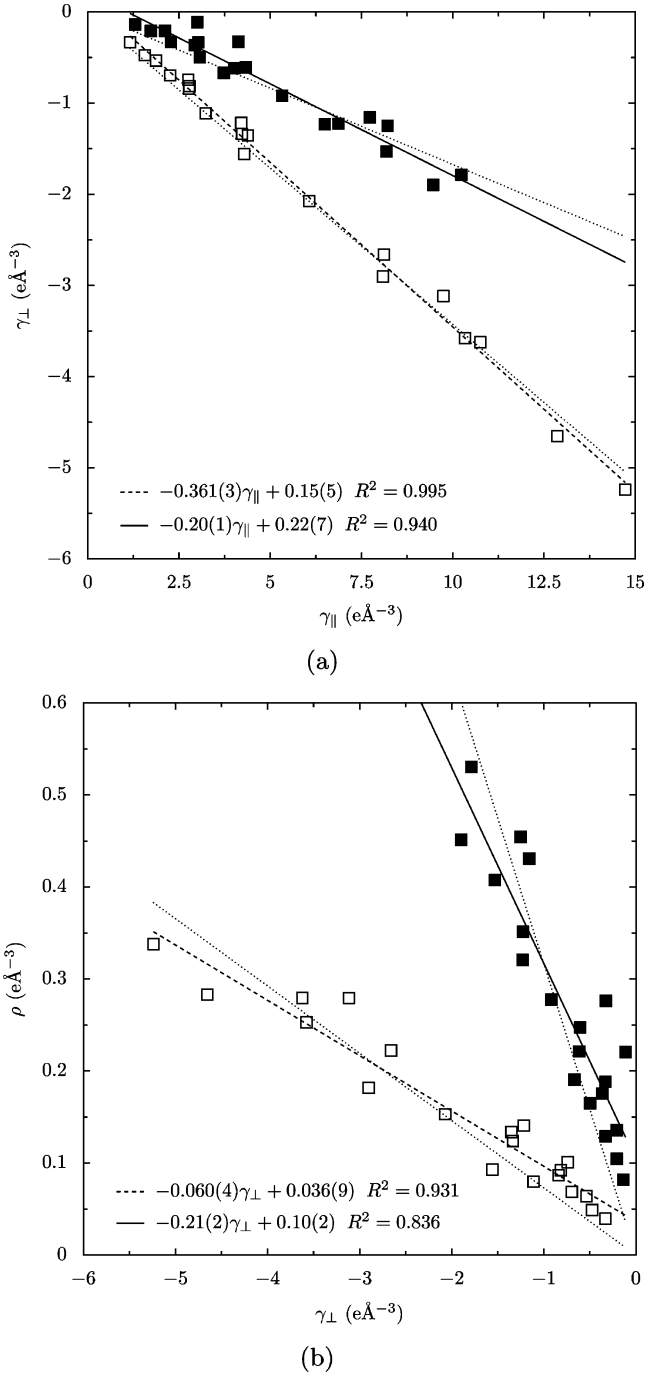

Figure 5. (a) $\gamma_\perp$ *vs* $\gamma_\parallel$ and (b) ρ *vs* $\gamma_\perp$ at φ-BCP (black symbols and solid line) and ρ-BCP (white symbols and dashed line). Dotted lines represent linear fittings without independent parameters.

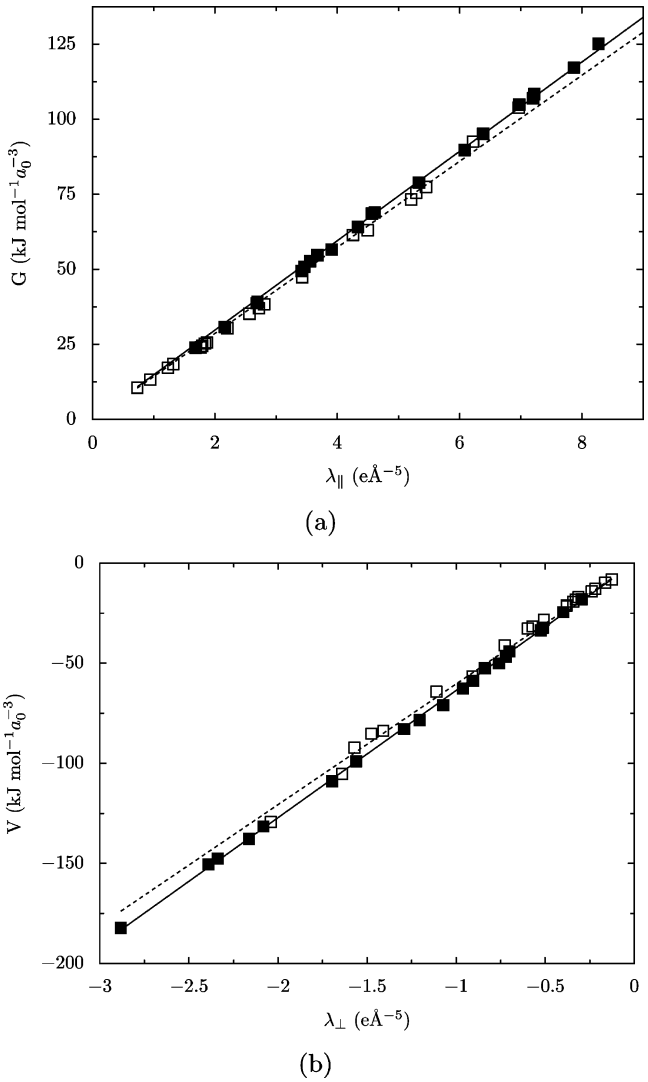

Figure 6. (a) G *vs* $\lambda_\parallel$ and (b) V *vs* $\lambda_\perp$ at φ-BCP (black symbols and solid line) and at ρ-BCP (white symbols and dashed line). Linear functions fitted to the complexes are: $G = 14.89(4)\lambda_\parallel$ and $V = 63.5(2)\lambda_\perp$ at φ-BCP, and $G = 14.3(1)\lambda_\parallel$ and $V = 60.3(7)\lambda_\perp$ at ρ-BCP.

d_{NH}. Thus, the expected proportionality between $\gamma_\perp$ and ρ is difficult to retrieve, as the effect of the environment increases the scattering around the line. Moreover, the environment effects on $\gamma_\perp$ and ρ are expected to be correlated *via* eq 2, which would affect the form of the dependences between these magnitudes.

3.3. Topological Properties of the Electron Density. The behavior of the topological and energetic properties of $\rho(\mathbf{r})$ at φ-BCP is analogous to that observed at ρ-BCP.[13,44] Indeed, besides the magnitude of ρ, the curvatures of $\rho(\mathbf{r})$ in the directions parallel and perpendicular to the bond ($\lambda_\parallel$ and $\lambda_\perp$, respectively) along with the electron kinetic (G) and potential (V) energy densities at φ-BCP decay exponentially with the distance, exhibiting similar correlation factors than at ρ-BCP (Table 3). In addition, at φ-BCP, $\nabla^2\rho$ is positive and decays in magnitude as d_{NH} increases, and the total electron energy density H exhibits a negative magnitude that also decreases when lengthening the interaction, becoming positive for the longest calculated d_{NH} distances. In both cases, the behavior is too complex to be fitted to a single exponential. It must be noticed that, for a given complex, the sign of the energy density H can change from ρ-BCP to φ-BCP.

At ρ-BCP the curvatures of $\rho(\mathbf{r})$, $\lambda_\parallel$ and $\lambda_\perp$, are found respectively proportional to G and V.[15] According to these relationships, $\lambda_\perp$ is related to the concentration of the electron distribution in the bonding region, as resulting from the formation of the complex, while $\lambda_\parallel$ reflects the depletion of $\rho(\mathbf{r})$ for a closed-shell interaction due to the repulsion between electrons, as stated by Pauli's principle for this kind of interaction. Similar proportionalities also hold at φ-BCP, with similar correlation factors (for G and V, $R = 0.9998$ and 0.9997 at φ-BCP, and $R = 0.9988$ and 0.9975 at ρ-BCP, respectively) (Figure 6).

Close to φ-BCP, the action of the electric field on the polarization of $\rho(\mathbf{r})$ is qualitatively different along the bond axis and in the perpendicular plane to that direction. Thus, along the hydrogen bond direction, the electron distribution at both sides of φ-BCP is polarized in opposite directions by the

electrostatic force, while outside the interaction direction the electrostatic force press the electron distribution toward the bond axis. In this way, $\rho(\mathbf{r})$ adapts to this situation by increasing the parallel and the perpendicular curvatures at φ-BCP, which become sharper. Outward φ-BCP, the opposite electrostatic forces on $\rho(\mathbf{r})$ along the parallel direction depletes the electron distribution, thus increasing the kinetic energy, while in the perpendicular direction the electrostatic force has a concentrating effect increasing the potential energy.

4. Conclusions

The electrostatic potential in hydrogen-bonding regions presents similar topological features than the electron density distribution. Through topological analysis, $\varphi(\mathbf{r})$ provides complementary information to $\rho(\mathbf{r})$, in particular concerning the effect of electrostatic forces on the bond. For both scalar fields a critical point is observed in the hydrogen-bonding region, indicating that each $\varphi(\mathbf{r})$ and $\rho(\mathbf{r})$ zero-flux surface separates this region in two parts. For $\rho(\mathbf{r})$, these parts are the atomic basins, while for $\varphi(\mathbf{r})$ they correspond to two enclosed regions (called finite φ-basins) where the integrated net charge vanishes. As $\varphi(\mathbf{r})$ closed zero-flux surfaces are impermeable to all the field lines growing inside and outside the enclosed region, φ-basins can be regarded as electrostatically isolated regions.

The φ and ρ zero-flux surfaces divide the N···H internuclear space in three regions: region I is limited by the φ-surface and contains the N-nucleus, region II is comprised between both zero-flux surfaces, and region III is limited by the ρ-surface and contains the H-nucleus. Thus, the φ-surface divides the N atom basin in regions I and II, the first one corresponding to the volume where $\rho(\mathbf{r})$ screens completely the N-nucleus. While region I has zero charge, region II is associated with the nitrogen lone-pair and presents a negative net charge that equals the magnitude of the positive charge of region III ($q_{II} + q_{III} = 0$) because regions II and III form a finite φ-basin. Therefore, the electrostatic pairwise N···H interaction involves these opposite charged regions, which define the electrostatic basin where the H-nucleus lies. It should be noted that, along the hydrogen-bonding direction, region II exhibits an almost constant size of ~13−14% of the d_{NH} distance for all studied complexes.

The topological analysis of $\varphi(\mathbf{r})$ is also helpful for deriving a further detailed description of $\rho(\mathbf{r})$ and the electrostatic forces involved in the interaction. Through diagonalization of the Hessian matrix at the critical points, three main curvatures of $\varphi(\mathbf{r})$ that have dimensions of electron density are obtained. As these curvatures are larger, the concentrating effect of the electrostatic forces exerted on $\rho(\mathbf{r})$ in the bonding region is larger. The split between the absolute value of the curvatures parallel ($\gamma_{||}$) and perpendicular ($\gamma_{\perp}$) to the bond is, according to Poisson's equation, proportional to the electron density magnitude and appears related to the repulsive forces from the electrons in the bonding region. At the critical points, the curvatures increase as d_{NH} decreases at the same exponential rate that ρ, being roughly proportional between them and to ρ. While $\gamma_{||}$ presents a clear exponential dependency and is mostly unaffected by the environment of the interaction, $\gamma_{\perp}$ and ρ present larger scattering around the exponential curve and depend more on the chemical complex.

Acknowledgment. The authors are very grateful to Dr. Carlo Gatti for helpful comments. E.E. also acknowledges Dr. Carlo Gatti for numerous fruitful discussions during his stay in the University of Nancy as an invited professor. This work was supported by the Spanish Ministerio de Educación y Ciencia (MEC) (Projects MAT2006-13572-C02-01 and CTQ2006-14487-c02-01/BQU). I.M. thanks also the MEC by a Juan de la Cierva fellowship.

Supporting Information Available: Tables of BCP calculation data. This material is available free of charge via the Internet at http://pubs.acs.org.

Note Added after ASAP Publication. This article was released ASAP on June 21, 2007. Equation 5 has been revised. The corrected version posted on July 5, 2007.

References and Notes

(1) Politzer, P.; Truhlar, D. G. *Chemical Applications of Atomic and Molecular Electrostatic Potentials*; Plenum Press: New York, 1981.
(2) Murray, J. S.; Sen, K. *Molecular Electrostatic Potentials*; Elsevier: Amsterdam; New York, 1996.
(3) Gadre, S. R.; Kulkarni, S. A.; Shrivastava, H. *J. Chem. Phys.* **1992**, *96*, 5253−5260.
(4) Leboeuf, M.; Köster, A. M.; Jug, K.; Salahub, D. R. *J. Chem. Phys.* **1999**, *111*, 4893−4905.
(5) Gadre, S. R.; Shrivastava, I. H. *J. Chem. Phys.* **1991**, *1991*, 4384−4390.
(6) Bader, R. F. W. *Atoms in Molecules—A Quantum Theory*; Clarendon Press: Oxford, U.K., and New York, 1990.
(7) Gadre, S. R.; Bendale, R. D. *Chem. Phys. Lett.* **1986**, *130*, 515−519.
(8) Politzer, P.; Parr, R. G.; Murphy, D. R. *J. Chem. Phys.* **1983**, *79*, 3859−3861.
(9) Wiener, J. J. M.; Grice, M. E.; Murray, J. S.; Politzer, P. *J. Chem. Phys.* **1996**, *104*, 5109−5111.
(10) Shuresh, C. H.; Koga, N. *J. Am. Chem. Soc.* **2002**, *124*, 1790−1797.
(11) Tsirelson, V. G.; Avilov, A. S.; Lepsehov, G. G.; Kulygin, A. K.; Stahn, J.; Pietsch, U.; Spence, J. C. H. *J. Phys. Chem. B* **2001**, *105*, 5068−5074.
(12) Bouhmaida, N.; Dutheil, M.; Ghermani, N. E.; Becker, P. *J. Chem. Phys.* **2002**, *116*, 6196−6204.
(13) Espinosa, E.; Molins, E.; Lecomte, C. *Chem. Phys. Lett.* **1998**, *285*, 170−173.
(14) Espinosa, E.; Alkorta, I.; Rozas, I.; Elguero, J.; Molins, E. *Chem. Phys. Lett.* **2001**, *336*, 457−461.
(15) Espinosa, E.; Lecomte, C.; Molins, E. *Chem. Phys. Lett.* **1999**, *300*, 745−748.
(16) Boyd, R. J.; Choi, S. C. *Chem. Phys. Lett.* **1985**, *120*, 80−85.
(17) Boyd, R. J.; Choi, S. C. *Chem. Phys. Lett.* **1986**, *129*, 62−65.
(18) Espinosa, E.; Molins, E. *J. Chem. Phys.* **2000**, *113*, 5686−5694.
(19) Espinosa, E.; Alkorta, I.; Elguero, J.; Molins, E. *J. Chem. Phys.* **2002**, *117*, 5529−5542.
(20) Espinosa, E.; Alkorta, I.; Mata, I.; Molins, E. *J. Phys. Chem. A* **2005**, *109*, 6532−6539.
(21) Umeyama, H.; Morokuma, K. *J. Am. Chem. Soc.* **1977**, *99*, 1316−1332.
(22) Møller, C.; Plesset, M. S. *Phys. Rev.* **1934**, *46*, 618−622.
(23) Frisch, M. J.; et al. *Gaussian 03, RevisionC.02*; Gaussian, Inc.: Wallingford, CT, 2004.
(24) Biegler-König, F.; Bader, R.; Tang, T.-H. *J. Comput. Chem.* **1982**, *3*, 317−328.
(25) Popelier, P. L. A. *MORPHY98, a topological analysis program, 0.2*; 1999.
(26) Alkorta, I.; Picazo, O. *Arkivoc* **2005**, *ix*, 305−320.
(27) Legon, A. C.; Millen, D. J.; Rogers, S. C. *Proc. R. Soc. London, Ser. A* **1980**, *370*, 213−237.
(28) Buxton, L. W.; Campbell, E. J.; Flygare, W. H. *Chem. Phys.* **1981**, *56*, 399−406.
(29) Legon, A. C.; Campbell, E. J.; Flygare, W. H. *J. Chem. Phys.* **1982**, *76*, 2267−2274.
(30) Soper, P. D.; Legon, A. C.; Read, W. G.; Flygare, W. H. *J. Chem. Phys.* **1982**, *76*, 292−300.
(31) Altman, R. S.; Marshall, M. D.; Klemperer, W. *J. Chem. Phys.* **1983**, *79*, 57−64.
(32) Goodwin, E. J.; Legon, A. C. *J. Chem. Phys.* **1985**, *82*, 4434−4441.
(33) Fraser, G. T.; Leopold, K. R.; Nelson, D. D.; Tung, A.; Klemperer, W. *J. Chem. Phys.* **1984**, *80*, 3073−3077.
(34) Fraser, G. T.; Leopold, K. R.; Klemperer, W. *J. Chem. Phys.* **1984**, *80*, 1423−1426.
(35) Jaman, A. I.; Germann, T. C.; Gutowsky, H. S.; Augspurger, J. D.; Dykstra, C. E. *Chem. Phys.* **1991**, *154*, 281−289.

(36) Legon, A. C.; Wallwork, A. L.; Fowler, P. W. *Chem. Phys. Lett.* **1991**, *184*, 175−181.
(37) Pathak, R. K. *J. Chem. Phys.* **1990**, *93*, 1770−1773.
(38) Johnson, R. D., III, Ed. *NIST Computational Chemistry Comparison and Benchmark Database, NIST Standard Reference Database Number 101 Release 12*, 2005; http://srdata.nist.gov/cccdbd.
(39) Gadre, S. R.; Badhane, P. K. *J. Chem. Phys.* **1997**, *107*, 5625−5627.
(40) Lakshmi, B.; Samuelson, A. G.; Jovan-Jose, K. V.; Gadre, S. R.; Arunan, E. *New J. Chem.* **2005**, *29*, 371−377.
(41) Tal, Y.; Bader, R. F. W.; Erkku, J. *Phys. Rev. A* **1980**, *21*, 1−11.
(42) Ziesche, P.; Gräfenstein, J.; Nielsen, O. H. *Phys. Rev. B* **1988**, *37*, 8167−8178.
(43) Bader, R. F. W.; Essén, H. *J. Chem. Phys.* **1984**, *80*, 1943−1960.
(44) Espinosa, E.; Souhassou, M.; Lachekar, H.; Lecomte, C. *Acta Crystallogr.* **1999**, *B55*, 563−572.